IOP Publishing Journal of Micromechanics and Microengineering
J. Micromech. Microeng. **21** (2011) 115014 (11pp) doi:10.1088/0960-1317/21/11/115014

Rapid nano impact printing of silk biopolymer thin films

Robert D White[1], Caprice Gray, Ethan Mandelup, Jason J Amsden, David L Kaplan and Fiorenzo G Omenetto

Tufts University, Medford, MA 02155, USA

E-mail: r.white@tufts.edu

Received 6 July 2011, in final form 22 August 2011
Published 12 October 2011
Online at stacks.iop.org/JMM/21/115014

Abstract
In this paper, nano impact printing of silk biopolymer films is described. An indenter is rapidly accelerated and transfers the nanopattern from a silicon master into the silk film during an impact event that occurs in less than 1 ms. Contact stresses of greater than 100 MPa can be achieved during the short impact period with low power and inexpensive hardware. Ring shaped features with a diameter of 2 μm and a ring width of 100–200 nm were successfully transferred into untreated silk films using this method at room temperature. Mechanical modeling was carried out to determine the contact stress distribution, and demonstrates that imprinting can occur for contact stresses of less than 2 MPa. Thermal characterization at the impact location shows that raising the temperature to 70 °C has only a limited effect on pattern transfer. Contact stresses of greater than approximately 100 MPa result in excessive deformation of the film and poor pattern transfer.

(Some figures in this article are in colour only in the electronic version)

Introduction

Silk biopolymers offer many attractive features for micro- and nano-scale devices. These materials are biocompatible, exhibit high mechanical toughness and excellent optical clarity, and can be formed into a variety of structures including thin films, fibers, fiber mats, gels, and foams [1–5]. In addition, the constructs have the ability to immobilize a variety of biochemical agents including enzymes and proteins, and maintain their activity over the course of years [6–8]. As an added benefit, silk processing is relatively benign, occurring in an aqueous environment at neutral pH and ambient temperatures.

The transfer of nanoscale patterns into silk films is of interest for a variety of biophotonic devices that include optical sensors, optical waveguides, tissue engineering scaffolds, and neural electrode arrays (e.g. [1–11]). Pattern transfer of nanoscale features into silk films has been demonstrated recently using both micromolding and nanoimprinting methods. For example, in [9], the authors demonstrate the ability to cast nanoscale patterns with 30 nm resolution in silk using soft lithographic micromolding techniques, with an emphasis on optical systems. Micromolding is a relatively slow method of pattern transfer, requiring hours to complete. Nanoimprinting is a faster alternative to micromolding for processing polymers at the nanoscale. In nanoimprinting, nanopatterns are generated by pressing a polymer film into a rigid stamp [12, 13]. The technique allows rapid reproduction of structures with 10 nm precision, and is a candidate to replace optical lithography in semiconductor processing. The technique has been most heavily studied for polymethylmethacrylate (PMMA) films [14]. Extending the technique to biopolymers is of interest, particularly for biomedical applications. For example, recent work has demonstrated the ability to nanoimprint 100 nm features into the biopolymer chitosan [15]. The first results for nanoimprinting into a silk biopolymer were reported in 2010 [10, 11]. In both papers, the authors were able to demonstrate the transfer of patterns with dimensions of the order of 100 nm into silk films at temperatures of 80–100 °C and contact pressures of less than 0.35 MPa (50 psi) for times of the order of 5 s.

In this work, we explore the possibility of increasing the pattern transfer rate using very rapid (<20 ms) nano impact printing. In nano impact printing, the pattern is transferred

[1] Author to whom any correspondence should be addressed.

 © 2011 IOP Publishing Ltd Printed in the UK & the USA

primarily by the high forces evolved during the impact of an indenter into the film. The impact event itself occurs on time scales of less than a millisecond. The entire process of impact printing including accelerating the indenter to the impact velocity and bringing the indenter back up into the print head occurs in less than 100 ms. Very high contact stresses (>100 MPa) can be achieved during the short impact period. To the best of our knowledge this paper is the first demonstration of nano impact printing of any kind. Ring shaped features with a diameter of 2 μm and a ring width of the order of 100–200 nm were successfully transferred into untreated silk films using this method at room temperature, with contact stresses of less than 2 to 100 MPa. Contact stresses of greater than approximately 100 MPa result in excessive deformation of the film and poor pattern transfer. A novel imprinting apparatus and method of manufacturing silicon nano features for the impact stamp are also described. The large contact stresses that can be achieved in nano impact printing may be an advantage in some applications, but may be a disadvantage in other applications. The magnitude of the impact stresses can be controlled through the design of the imprinting apparatus. This paper describes the contact and impact mechanics in detail to assist in the design process.

Material processing

Silk fibroin solutions were prepared from *Bombyx mori* cocoons through a process that has been described in detail elsewhere [16]. The process removes the sericin binding protein from the silk cocoon, dissolves the fibroin in LiBr, and then replaces the LiBr with deionized water through a dialysis process, resulting in a solution of silk fibroin in water. Silk fibroin thin films were then prepared by drying 9% wt/vol silk fibroin solution in a petri dish for 24 h at room temperature and ambient humidity (approximately 22 °C, 50% RH). Care was taken to level the dish with respect to gravity to ensure thickness homogeneity of the drying film. Seven milliliters of silk solution was used in each 100 mm diameter dish, resulting in optically clear films of 101 $\pm$ 9 μm thickness, as measured with a micrometer.

Once dried, the films are easily detached from the dish, cut to size, and mounted onto a rectangular acrylic frame using doubleside tape (Catalog #137, 3 M, St Paul, MN). The frame is mounted into the custom rapid imprinting setup shown in figure 1. The impact printing setup is comprised of a Cimarec hotplate, on which is mounted an aluminum baseplate, secured tightly to the hotplate with mounting screws and thermally connected with thermal grease. A silicon stamp is held in the center of the baseplate by a vacuum system. A type K thermocouple is mounted in a hole which extends to the center of the baseplate, just below the silicon stamp. An 80/20 aluminum frame holds a computer controlled MTS50 XY micropositioning stage with 50 mm travel (Thorlabs, Newton, NJ). The stage mounts to the frame holding the silk film, and can position the film relative to the indenters and silicon stamp. The indenters are miniature single acting air cylinders with a return spring. The five indenters each have 1.6 mm diameter shafts, terminated with

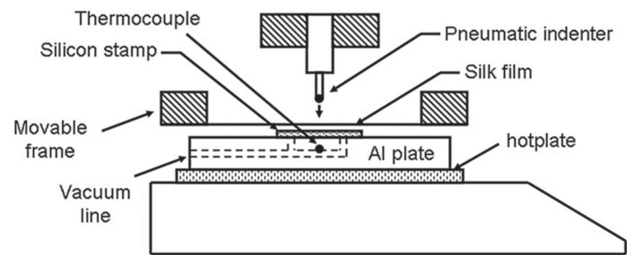

Figure 1. Schematic of the rapid imprinting setup.

a hemispherical epoxy bump which provides the imprinting surface (Devcon S-31/31345, ITW Performance Polymers, Riviera Beach, FL). The hemispherical bump is important to give a smooth impact surface, and also allows a range of stresses to be evaluated during a single impact, as explained below in the discussion of contact mechanics. The air cylinders are individually controlled via solenoid valves driven by a regulated air compressor. The impact velocity of the cylinders is controlled by changing the regulated air pressure, using a ControlAir Inc Type 500X E/P transducer driven from the computer by an analog control voltage. For rapid nano impact printing, the pressure is first set to the desired value, and the solenoid valve is opened, allowing the most rapid possible rise in pressure.

Computer control and measurement, including temperature measurement via the thermocouple, control of the micropositioning stages, and timed control of the air cylinder imprinters are accomplished using the NI USB-6008 multifunction DAQ and Labview control software (National Instruments, Austin, TX) with appropriate power amplifiers. This custom setup allows very short imprint times through computer control of the low-inertia indenters with good knowledge of temperature and pressure.

The silicon stamp used as the master surface to imprint the film was manufactured using surface micromachining techniques. The starting substrates were ⟨1 0 0⟩ oriented, p-type (1–10 Ω cm) silicon wafers. Shipley S1813 photoresist was spun onto an 800 nm thickness and patterned via an optimized UV contact lithography process. The mask pattern used consisted of 2 μm squares arrayed on a 4 μm center-to-center pitch. After lithography, the corners of the squares were rounded off by diffraction to form approximately 2 μm diameter circles on a 4 μm pitch. The wafer was etched in an SF_6 plasma using a parallel plate RIE etcher at 80 mT and 150 W, for a silicon etch rate of 240–415 nm min^{-1} (the etch rate varied with radial position; it is faster near the edge), and a photoresist etch rate of approximately 250 nm min^{-1}. The samples were etched for 5 min. This intentional overetch completely removed the resist as well as etching down into the silicon. Any remaining resist residue was then removed using a high power O_2 plasma, and the wafers were subdiced to produce the final nanoimprinting stamp.

The SF_6 overetch allowed the production of features below the diffraction limit of the NUV aligner. The resist is somewhat (hundreds of nanometers) thicker around the edge of the 2 μm circles than the center. Thus, by overetching the sample,

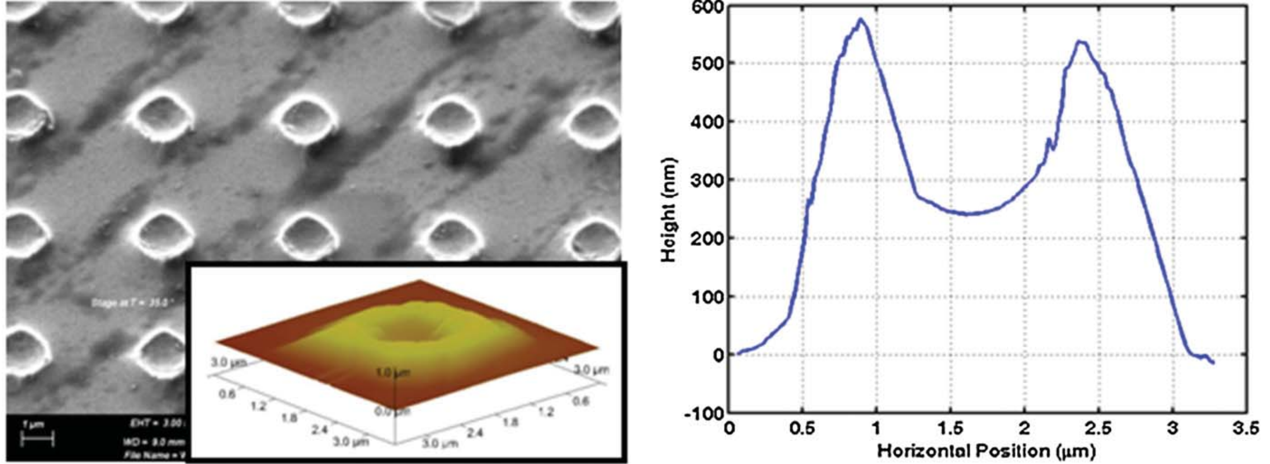

Figure 2. The silicon stamp produced by overetching of the silicon surface in an SF_6 plasma. (Left) SEM image showing the array of craters, and (inset) AFM image showing an individual nanocrater. (Right) cross-section from the AFM image through the center of the nanocrater.

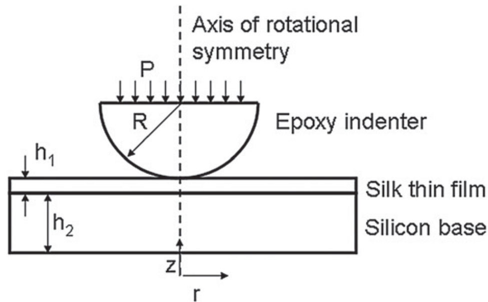

Figure 3. Schematic of the contact mechanics problem.

the combination of undercut and resist thickness variation allows the production of circular 'crater'-like structures with a 2 μm diameter and a sharp 600 nm high 'rim'. The rim starts at approximately 500 nm in width and tapers to a sharp edge less than 100 nm in width. The precise shape of these structures varies over the wafer, due to radial nonuniformity in the etch rates. However, in a given millimeter sized region, the structures are uniform. Figure 2 shows scanning electron microscope (SEM) and atomic force microscope (AFM) images of the silicon stamp structure in the region in which the nanoindentation experiments were performed. Of the order of 50 impact experiments were conducted at the same location in the silicon stamp. No degradation of the silicon stamp was observed. The AFM and SEM images in figure 2 were taken after the impact experiments had been conducted.

Quasistatic contact mechanics

Figure 3 shows a schematic of the contact mechanics occurring between the hemispherical indenter and the silk film. The silicon stamp is on the bottom side of the silk film. Force applied to the top of the indenter by air pressure causes the indenter to press the silk into the silicon stamp. Transfer of the nanopattern from the stamp to the silk film depends on the radial distribution of the contact stress at the silk/silicon interface. This problem has some similarities to the Hertzian contact problem between an elastic hemispherical indenter and an elastic half space [17–19]. In the classic Hertzian solution, the contact stress is

$$\sigma(r) = \frac{3P}{2\pi a^3}\sqrt{a^2 - r^2}, \qquad (1)$$

where P is the total applied load, r is the radial coordinate, and a is the radius of the contact region,

$$a = \left[\frac{3R\left[E_1\left(1-\upsilon_2^2\right) + E_2\left(1-\upsilon_1^2\right)\right]}{4E_1E_2}P\right]^{1/3}, \qquad (2)$$

where R is the radius of the indenter, and E_1, ν_1, E_2, and ν_2 are the elastic moduli and Poisson ratios for the indenter and the substrate. The Hertzian solution was compared to the finite element solution for low contact loads on the top surface, and matched precisely, validating the finite element analysis (FEA) result at low loads.

However, four major features distinguish the situation described in this paper from the Hertzian contact problem. First, and most significantly, the indenter is traveling with substantial velocity prior to impact, and the forces required to decelerate the inertia of the moving indenter substantially exceed the static contact stresses. Second, the stresses are large enough to exceed the yield stress limit of the silk film, and possibly that of the epoxy indenter. Third, the stress of interest is at the bottom of the silk film, and not at the surface being indented. Finally, the three layer structure with the stiff substrate (the silicon stamp) has an influence on the mechanics.

Thus, in order to determine the expected contact stress distribution between the silk film and the silicon stamp, a finite element model was constructed. The FEA model is a 2D axisymmetric static continuum mechanics model with elastic/perfectly plastic material models. Abaqus CAX4H four-node bilinear axisymmetric quadrilateral elements were used with a constant pressure hybrid formulation. $R = 0.8$ mm

is the radius of the indenter, $h_1 = 100$ μm is the thickness of the silk film, and $h_2 = 100$ μm is the portion of the silicon stamp that is included in the analysis. This does not represent the full thickness of the silicon, which extends to more than 500 μm, but is of sufficient size to capture the deformed region of the silicon near the surface. An axisymmetric boundary condition is applied along the symmetry axis at $r = 0$. The base of the silicon at $z = 0$ has a fixed displacement boundary condition in both the z- and r-directions. A displacement boundary condition is applied to the top side of the epoxy indenter, moving the top surface uniformly downwards in a quasistatic fashion to a maximum displacement of 100 μm. The total applied load, P, is computed in post-processing by integrating the normal stress over the boundary at each step.

A surface-to-surface interaction is used to model the surface contact between the silk and the epoxy. The epoxy indenter is the master surface and the silk film is the slave surface. The mesh is a free quadrilateral mesh generated with an advancing front algorithm. The element size is biased with a 30:1 ratio toward the point of contact. Thirty elements are used in the z-direction in each of the three parts. 100 elements are used in the r-direction in the silicon and silk parts.

The elastic modulus and Poisson ratio of the silicon are taken to be $E_3 = 190$ GPa and $\nu_3 = 0.23$ [20, 21]. $E_1 = 2.07$ GPa, $\nu_1 = 0.4$, and $(E_1)_y = 78$ MPa are the elastic modulus, Poisson's ratio, and yield stress of the epoxy indenter. The compressive elastic modulus and yield stress were taken from the manufacturer's datasheets. The Poisson ratio is taken as the average value based on three different epoxies measured by Fermilab [22]. Although these epoxies differ somewhat from the epoxy used here, the measured Poisson ratios only vary over the small range of 0.36 to 0.43. In the Hertzian solution, such a variation would result in at most a 5% change in contact stress, in the worst case where the deformation was entirely limited to the epoxy.

$E_2 = 4.1$ GPa, $\nu_2 = 0.3$, and $(E_2)_y = 50$ MPa are the elastic modulus, Poisson's ratio and yield stress of the silk thin film. The Poisson ratio for silk thin films is an estimate following the argument of Pérez-Rigueiro *et al* [23]. The elastic modulus of the silk thin film was measured at 20 °C using tensile testing in an Instron Model 3366 uniaxial tensile tester with video extensometer and Biopuls$^{\mathrm{TM}}$ (Instron, Norwood, MA) pneumatic grippers. A 106 μm thick silk thin film was cut into a 'dogbone' shape with a 10 mm long, 3.2 mm wide test section expanding to wider ends for clamping. The sample was loaded at a strain rate of 0.1% strain per second to failure while monitoring the applied load. The resulting stress train curve is given in figure 4 below. The elastic modulus of the film is 4.1 GPa and the ultimate tensile strength is 50 MPa. Note that the tensile measurements of silk film properties presented here are 30% higher, but nearly within the error bounds, when compared with tensile measurements of untreated (air dried) silk fibroin thin films given elsewhere. For instance, Jiang *et al* and Noishi *et al* measure elastic moduli of 3 ± 1 GPa and ultimate tensile strengths of 30 ± 10 MPa [24, 25]. The ultimate tensile strength may not be identical to the compressive yield strength. However, this is the best estimate of the compressive yield strength available,

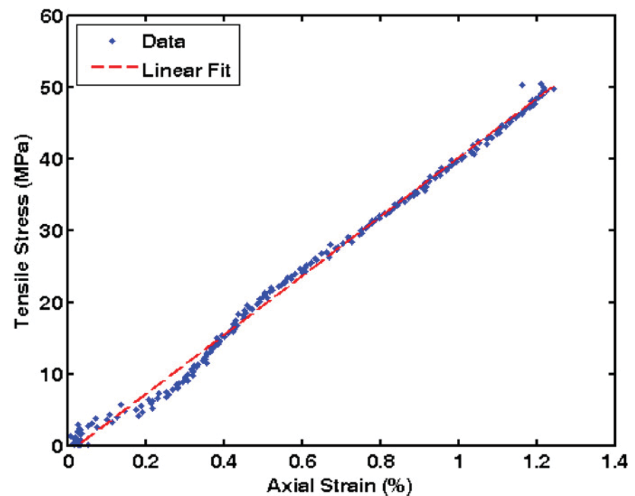

Figure 4. Silk film tensile testing results at 20 °C. Material is linear elastic with an elastic modulus of 4.1 GPa and an ultimate tensile strength of 50 MPa.

as no other consistent data have been generated to the author's knowledge for compressive yield strength of silk thin films of this type. Attempts made as part of this study to measure compressive yield strength by nanoindentation did not produce consistent results.

A result for the normal stress distribution in the z-direction, σ_{zz}, is shown in figure 5 below. The figure shows the region near the contact point. This particular result is for a total applied load of 0.3 N. At this load, plastic yielding has already occurred in a sub-surface region in the silk film.

From the finite element computations, we can extract both the total load verses displacement of the indenter, and the contact stress distribution at the bottom of the silk film where it interacts with the silicon stamp, as shown in figure 6. The predicted stress distribution at three different loads is also shown in figure 6. These three loads correspond to the maximum loads expected during impact for three different supply pressures (20, 25, and 40 psi), as computed below in the discussion of impact mechanics.

Force and velocity measurements

Force measurements were made prior to the imprinting experiments for each of the piston imprinters to determine the imprinting force. A Sensotec model 31 miniature load cell was used for this purpose (Honeywell Sensotec-Lebow, Columbus, OH). The sensor was first calibrated statically against standard weights to remove offset and sensitivity drift. The load cell was thread mounted into a test plate and placed at the same distance from the stage as the baseplate, with a piece of silicon and silk on top of the sensor to mimic the imprinting setup. Separate measurements were then carried out for each piston imprinter at five different supply pressures (20, 25, 30, 35, and 40 psi), and for various pressure rise times and dwell times (as shown in table 2). Repeatability was checked five times, and variation from piston to piston or run to run was noted. In the medium force case (1.0 N average force) run-to-run

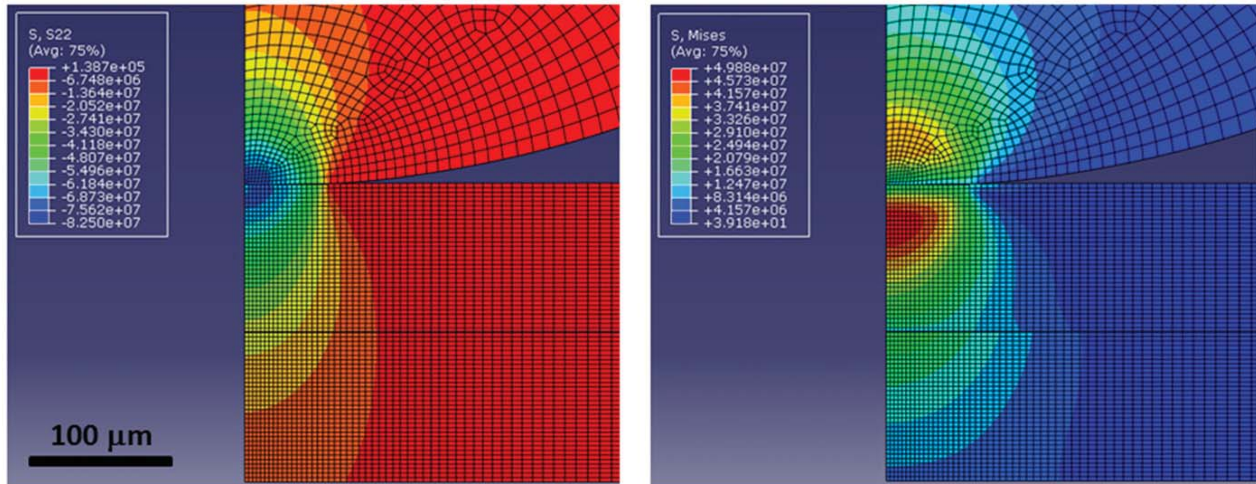

Figure 5. Abaqus result showing the stress field in the indenter and the silk films for a load of 0.3 N. (Left) normal stress in the z-direction. (Right) von Mises stress. Stresses are indicated in units of Pa.

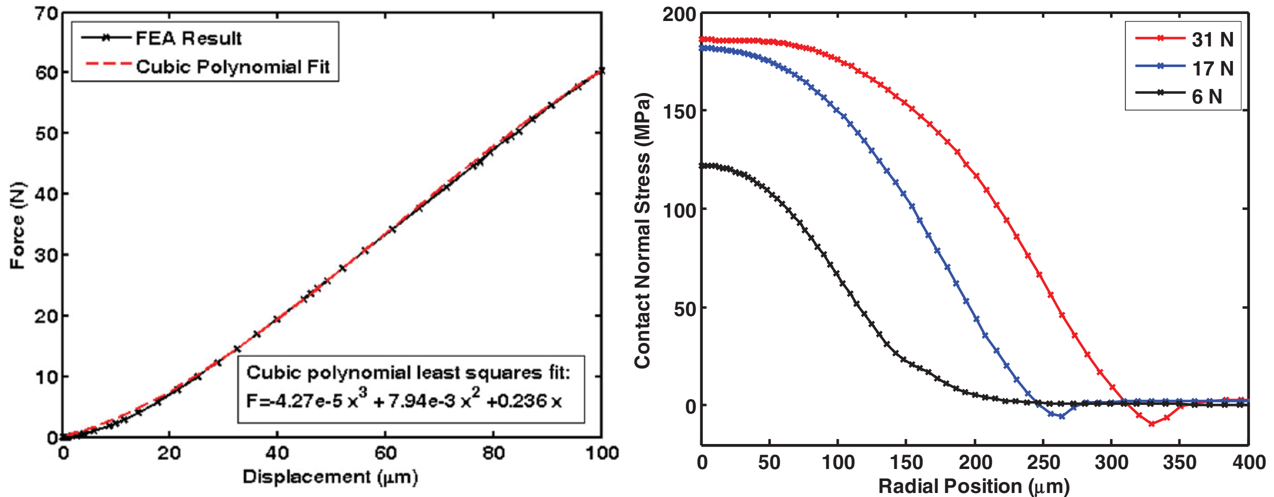

Figure 6. Finite element results showing (left) total force versus deflection of the top of the indenter (right) normal (z-direction) contact stress at the interface between the silk film and silicon stamp, for three different applied loads, as a function of radial position.

and piston-to-piston repeatability ($N = 5$) both have standard deviations of 0.06 N. Five force cases were run, with average forces of 0.26 ± 0.02, 0.63 ± 0.01, 1.00 ± 0.02, 1.36 ± 0.02 and 1.70 ± 0.02 N. The reported uncertainties are the standard deviation of the static force measurements for different rise times and dwell times ($N = 5$–8).

The total imprint dwell time (the time that the piston is statically in contact with the film following the impact) was also determined from the load cell data. Variation in imprint dwell time from run to run was less than 20 ms. The measured rise time and fall time were also approximately 20 ms. From the data, it is not directly known whether this is the actual force rise time or the rise time of the sensor; however, impact computations below suggest that there is a much larger impact force which occurs in times of less than 0.1 ms. This is not seen in the data, so it seems likely that the sensor rise time is of the order of 20 ms and it is incapable of capturing the high force impact event. Therefore, we can conclude from the measurements that the actual rise time during the impact is less than 20 ms, but no more precise timing data are available. The uncertainty in imprint time is taken to be the measured rise time: $\pm$ 20 ms.

For the impact imprinting case, the momentum of the imprinter just prior to contact with the film is of primary importance. This quantity depends on the moving mass of the imprinter and its velocity just prior to impact. One of the piston imprinters was cut apart, and the moving pin and piston assembly was massed on a precision balance yielding a value of 610 ± 1 mg. The velocity of the moving piston was measured using a non-contact laser displacement sensor, Keyence model LB-70W (Keyence Corporation, Osaka, Japan). The sensor has a 0.7 ms sample time, and is capable of measuring the distance to a reflecting object with a manufacturer specified precision of 0.18 mm. The total travel distance of the

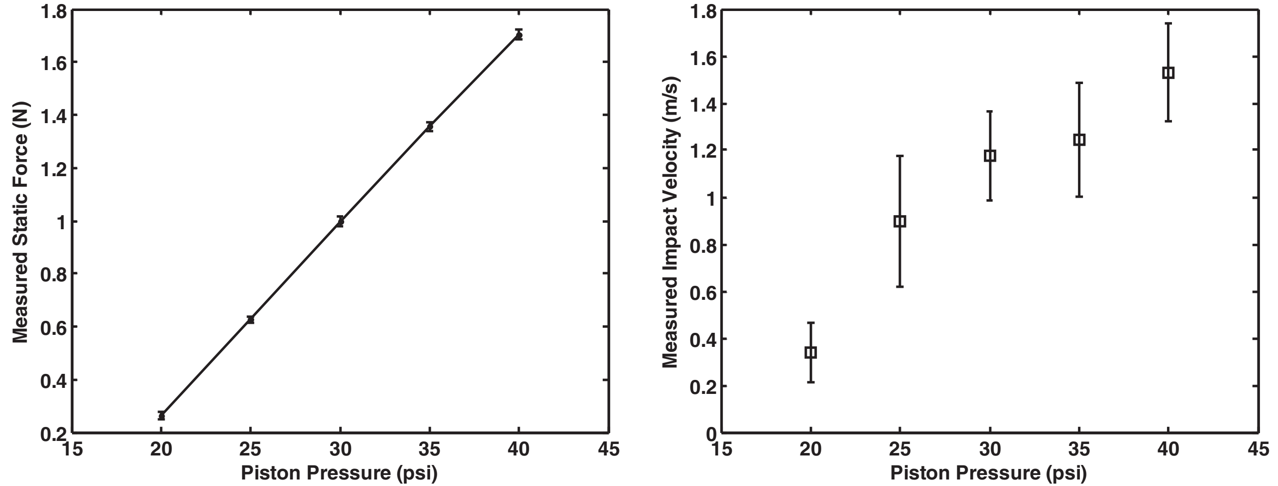

Figure 7. (Left) load cell measurements of static force for different supply pressures. (Right) laser measurements of the velocity of the indenter just prior to impact for different supply pressures.

piston is 11 mm. The piston was mounted sideways and the Keyence sensor was used to measure the position of the head during extension at the five different supply pressures (20, 25, 30, 35, and 40 psi) for the rapid rise time case (<20 ms force rise time). The analog voltage corresponding to displacement was captured with the computer DAQ system with a 10 kS s^{-1} sampling rate, and the resulting displacement results differentiated in post-processing to compute velocity. A four-point moving average was applied after differentiation to reduce numerically amplified noise. The velocity just before the piston reached the end of travel was recorded. Velocity was measured to be relatively constant over the second half of the travel distance of the piston, so the results should not be sensitive to the exact distance to the impact location. Variations in velocity over the course of piston travel and sensor noise contribute to approximately 0.2 m s^{-1} of uncertainty in the measurement. The impact velocities measured for the five supply pressures are 0.34 ± 0.13, 0.90 ± 0.28, 1.18 ± 0.19, 1.25 ± 0.24, and 1.53 ± 0.21 m s^{-1}. More variation in velocity is observed at low pressure levels. The results are consistent with the total travel distance for the piston, and show an increasing trend of velocity with pressure, lending a level of confidence to the results. The results for both static force and impact velocity are plotted against supply pressure in figure 7.

Impact mechanics

In nano impact printing, the film is indented primarily by the momentum transfer during the impact, rather than the static load. This can be seen by analyzing the measured velocity results in light of the expected load deflection characteristics of the film. In order for the indenter to decelerate from the impact velocity to rest, the full momentum of the indenter must be transferred to the film. In order to conserve momentum, however, we require that

$$m\ddot{x} = -F(x, \dot{x}), \tag{3}$$

where $m = 6.1 \times 10^{-4}$ kg is the moving mass of the piston, and F is the force applied by the substrate on the piston. Since the silk film deforms as the piston indents into it, F is a function of displacement of the top of the indenter, x. Since the polymer may exhibit viscoelastic properties, force may also be a function of velocity, $\dot{x}$. Rather than attempting to incorporate the temperature and hydration dependent viscoelastic properties of the silk films, as an approximation, we take the material to be elastic/perfectly plastic. We can then extract the force–displacement characteristics from the FEA shown in figure 6. A good fit to the FEA result, shown in figure 6, is

$$F(x) \approx (-4.27 \cdot 10^{-5})x^3 + (7.94 \cdot 10^{-3})x^2 + 0.236x, \tag{4}$$

where $F(x)$ is the force in newtons and x is the displacement in micrometers. If we numerically solve (3) with the initial velocity set to the measured impact velocity, we can arrive at an estimate of the total distance traveled by the indenter top as it decelerates, and hence the maximum restoring force, that occurs during the impact event. This is the distance traveled, x, time, t, and force, $F(x)$, at which the indenter velocity, $\dot{x}$, first goes to zero. The results of this computation are summarized in table 1.

Table 1. Results of impact mechanics calculation.

	Maximum indenter force occurs at		
Initial velocity (m s^{-1})	Time (ms)	Displacement (μm)	Force (N)
0.34	0.07	15	5.2
0.90	0.06	35	16
1.18	0.06	45	23
1.25	0.06	47	24
1.53	0.05	55	30

It is emphasized that this calculation is approximate, since the analysis does not include any viscoelastic energy dissipation mechanisms which may be present in the film, and also neglects the inertia of the film material and

Table 2. Nano impact printing parameters.

Parameter	Values	Uncertainty
Surface temperature (°C)	19, 38, 70	±2 °C
Dwell time (s)	0.1, 0.25, 0.5, 1, 2	±20 ms
Static imprint force (N)	0.26, 0.63, 1.00, 1.36, 1.70	±0.06 N
Impact velocity (m s^{-1})	0.34, 0.90, 1.18, 1.25, 1.53	±0.28 m s^{-1}

any resulting structural vibrations that may be generated. Such calculations cannot be carried out without significant additional characterization of the viscoelastic properties of the silk film.

The major result of this computation is that the momentum transfer results in much higher peak force (5.2–30 N predicted) than the static force (0.26–1.7 N measured). Thus, momentum transfer from the impact is expected to be the dominant mechanism for nano impact printing. This suggests that no change in imprint pattern should be observed for different dwell times. This is indeed what is observed experimentally. In addition, the impact calculation predicts that the impact event occurs in less than 0.1 ms. This is faster than the load cell can respond, which is of the order of 20 ms. Hence, as discussed previously, the load cell is not expected to register the large impact forces; it can only be used to measure the static load present during the static dwell.

Temperature measurement

Temperature measurements during processing were made using a K-type thermocouple embedded in the center of the aluminum baseplate below the silicon stamp (see figure 1). While it is convenient to measure the temperature at the plate center during processing, the relevant quantity is the surface temperature of the silicon stamp. In order to relate the two, an infrared (IR) emission measurement was made of the silicon stamp surface. A piece of silicon identical in dimensions to the stamp, but without surface nanopatterns, was cut and painted with a thin black film using DE1634 Dupli-Color low gloss black engine enamel (Dupli-Color Products, Cleveland, OH). This paint has been carefully characterized and has a hemispherical emissivity of 0.83 across a wavelength range of 1.5 to 50 μm at 32 °C. There is less than 1% change in emissivity from 32 to 102 °C, translating to less than 1% error in measured temperature across that range.

A Fluke 62 Mini IR Thermometer was used to measure the temperature of the painted silicon (Fluke Corp., Everett, WA). The latter device assumes an emissivity of 0.95. After correcting for the actual emissivity of the material (which creates a 3.4% increase in actual temperature over measured temperature), the surface temperature of the silicon stamp is measured to be 38 °C for a thermocouple reading (inside the baseplate) of 45 °C, and 70 °C for a thermocouple reading of 75 °C. Based on manufacturer error bounds, the IR thermometry measurements are expected to be accurate to within 2 °C. Note that these temperatures are significantly below the front panel temperature indicated on the hotplate of 60 and 105 °C, respectively. This is not unexpected, as there is a substantial structure in between the top surface of the plate and the imprinting stamp. Nano impact experiments were conducted with the silk film initially at these two temperatures in addition to room temperature tests.

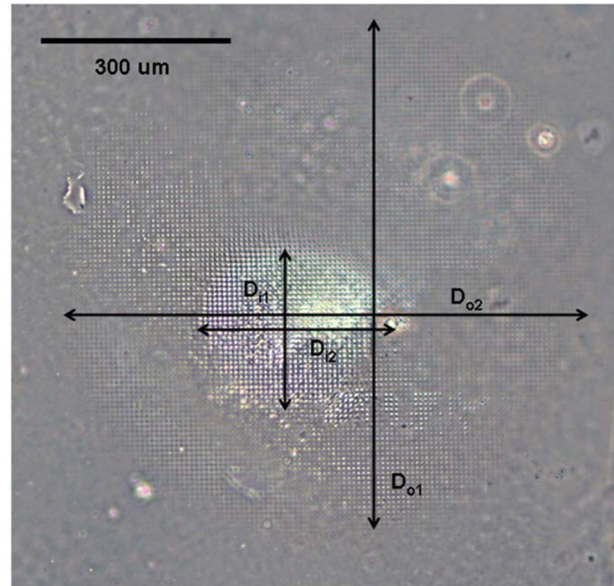

Figure 8. Light microscope picture (transmitted light, darkfield illumination) showing the diameters of the outer and inner imprinted regions for a 1.2 m s^{-1}, 38 C impact print. This is a typical result.

Local transient temperatures near the impact may be elevated above the static temperature maintained by the hotplate. Since the collision is inelastic, much of the kinetic energy is transformed into thermal energy. This will cause a local rise in the temperature of the film near the impact site. The total kinetic energy of the indenter is known prior to impact. In order to gain a sense for the possible temperature change, consider the highest velocity case, where the kinetic energy just prior to impact is 0.7 mJ. No diffusion calculations were conducted, but if all of this energy were used to raise the temperature of a 100 μm cube near the impact site, the temperature would rise approximately 440 °C, taking the silk film volumetric heat capacity to be approximately 1.6 J K^{-1} cm^{-3} [26]. No independent measurements of local temperature change or detailed thermal analyses were carried out in this study, nor were any local changes in the silk film properties measured. However, the potential for substantial local temperature rise in the region of the impact is noteworthy and warrants further study, particularly if the silk film is to be doped with thermally sensitive agents.

Nano impact printing results

Temperature, static dwell time, and supply pressure (which influences both impact velocity and static load) were varied. All permutations of the process variables appearing in table 2 were tested. Note that the static imprint force and impact velocity were not varied independently, as they vary together in response to the supply pressure.

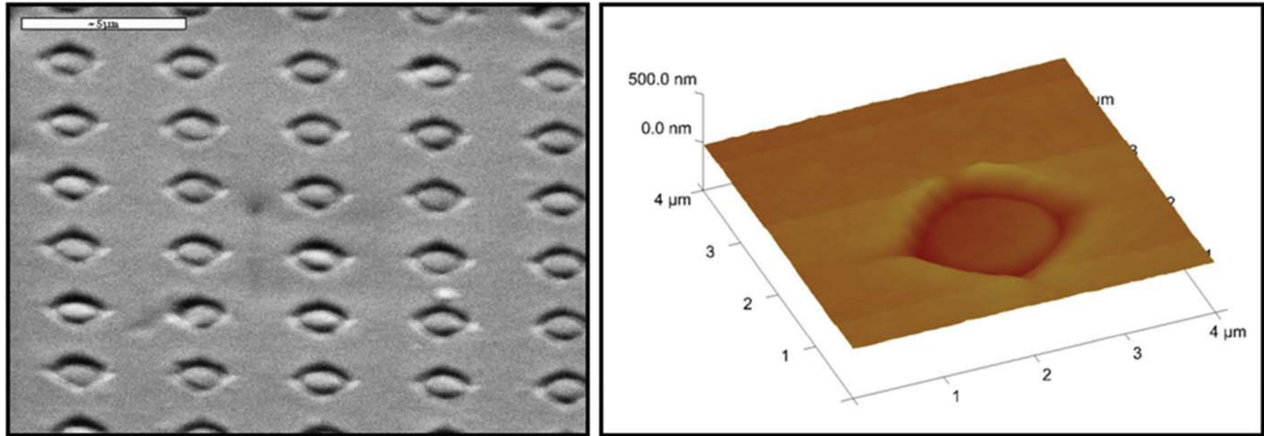

Figure 9. Images of the silk film after impact printing in the outer region, where good pattern transfer is experienced. Results are for a 1.2 m s, 38 C impact print. This is a typical result. (Left) SEM image; (right) AFM image.

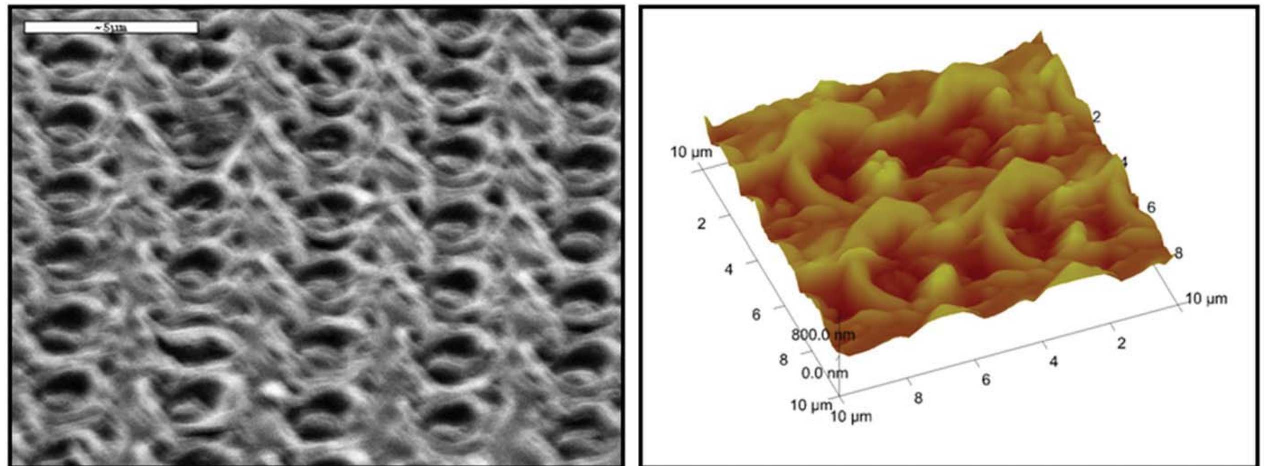

Figure 10. Images of the silk film after impact printing in the inner region, where poor pattern transfer is experienced. Results are for a 1.2 m s^{-1}, 38 C impact print. This is a typical result. (Left) SEM image; (right) AFM image.

After impact printing, the films were first examined under a light microscope using transmitted white light and darkfield illumination. For all nano impact printing cases, pattern transfer was successful. A typical image is seen in figure 8. There are two regions of the pattern that can be seen. In the center, there is an inner region that appears bright in the light microscope image due to large amounts of scattered light from the darkfield illumination. This inner region has a certain radius, determined by measuring the two orthogonal diameters, D_{i1} and D_{i2}, as shown in the figure and taking half their average. There is also an outer imprinted region that is not as clearly seen, but can be made out in the darkfield image. This has a larger radius, determined in similar fashion.

SEM and AFM images of the nano impact prints in the two regions are shown in figures 9 and 10. In the outer region, pattern transfer from the stamp is good and the in-plane geometry of the stamp pattern is faithfully reproduced in the silk film. In the inner region, pattern transfer is poor; the silk material is excessively deformed and no longer follows the pattern in the stamp. These two regions are indicative of the process window for applied contact stress. Contact stresses are larger in the inner region, and have exceeded a maximum threshold above which deformations are larger than the features of the stamp. In the outer region contact stresses are large enough to create pattern transfer, but not so large as to generate excessive deformation. The window of contact stresses experienced by the outer region is desirable for good pattern transfer.

The measured inner and outer radii for all permutations of the process variables are shown in figure 11. Three plots are shown. In each plot, the mean radius is plotted verses one of the three process variables. The mean is taken across all results for the other two process variables. The standard deviation across these same two process variables is expressed in the form of error bars. So, for example, in the 20 °C case the mean and standard deviation are across all dwell times and all impact velocities for a total of $N = 25$ (as 5 impact velocities and 5 dwell times were tested). Hence, the error bars do not express uncertainty in the measurement; rather, they express variation across the secondary process variables.

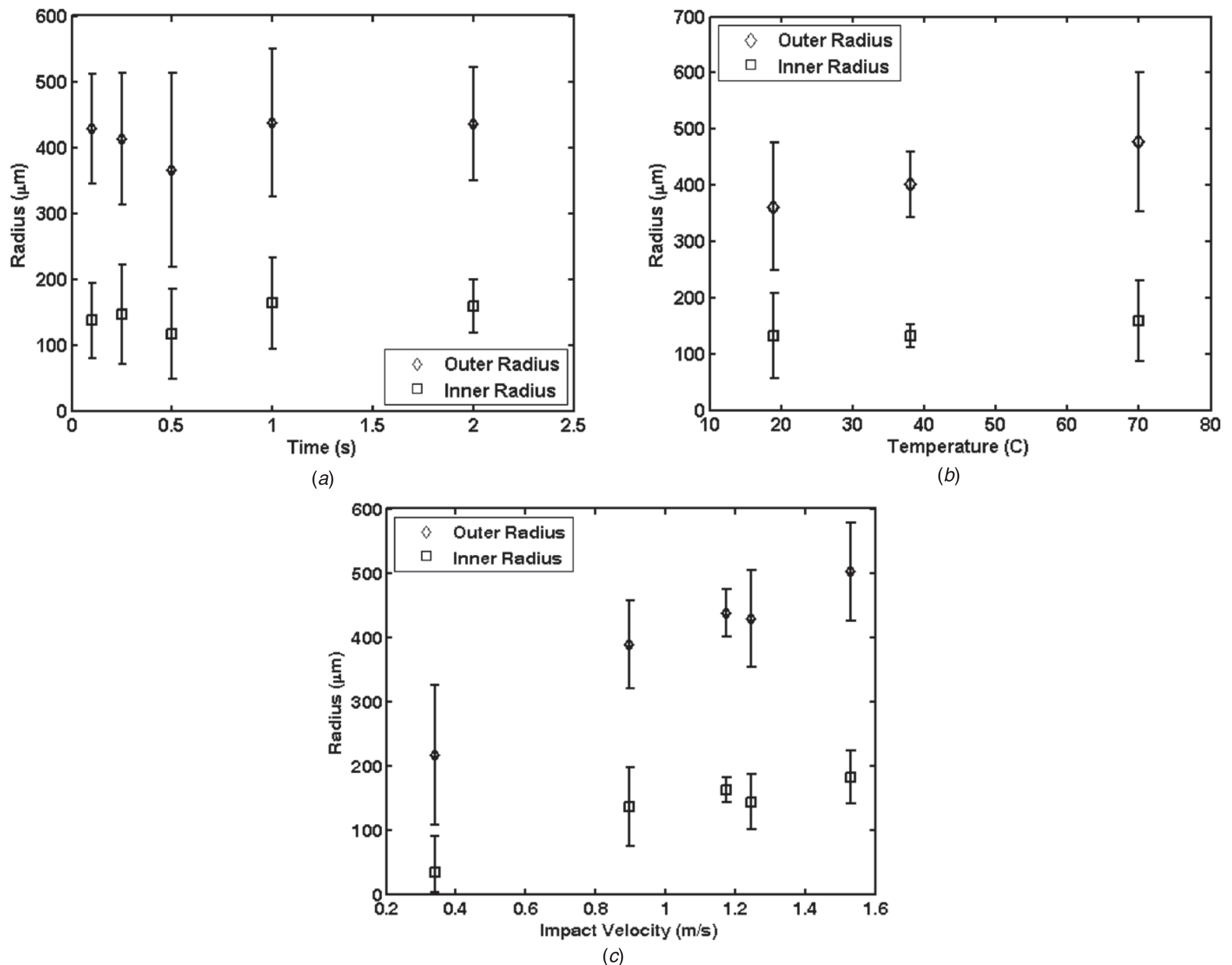

Figure 11. Results of parameter variation on the inner and outer radii of the successfully nano impact printed region.

Discussion

By using a hemispherical indenter, it is possible to examine a range of contact stresses in one experiment. Stress varies with radial position as shown in figure 6. The range of radii over which successful pattern transfer occurs maps directly onto a window of acceptable contact stresses.

First, consider the dwell time process variable. As can be seen in figure 11(*a*), no significant variation in either the inner or outer radii is observed while varying dwell time. This is consistent with the expectation that pattern transfer occurs during the rapid impact event. The much lower stresses present during quasistatic loading have no observable influence on the pattern. The results here show that the entire impact print process, including accelerating and retracting the indenter, can occur in 100 ms, a very rapid transfer process.

Second, consider the temperature process variable. Temperature has a small, but measurable, effect on the pattern transfer region. As can be seen in figure 11(*b*), the inner radius is not strongly affected by increasing the temperature, but the mean outer radius of the impact printed region increases from 370 μm at room temperature to 470 μm at 70 °C. This suggests that the silk modulus and/or yield strength reduce with temperature. Note also that the radius of the inner region does not change significantly with temperature; it remains constant at approximately 150 μm. Thus, raising the temperature increases the size of the process window, particularly at the low end of the stress range (below 5 MPa). However, impact printing occurs successfully at room temperature with a wide process window.

Finally, consider the impact velocity process variable. As can be seen in figure 11(*c*), both the inner and outer radii of the impact printed region increase with increasing impact velocity. This is consistent with the implicit assumption that contact stress is the controlling parameter. By comparing the inner radius to FEA computations of the contact stress, the maximum allowable contact stress can be determined. The inner radius varies from 40 μm for the lowest velocity case to 180 μm for the highest velocity case. The impact calculations and FEA results suggest that this corresponds to approximately 100–125 MPa of contact stress. Thus, at contact stresses above this level for all cases the pattern transfer is significantly distorted.

The outer radius varies from 210 μm for the lowest velocity case to 500 μm for the highest velocity case. FEA calculations for the lowest impact velocity case indicate that the contact stress at a radius of 210 μm is approximately 4 MPa. For the highest impact velocity case, the FEA calculations suggest that the contact stress at a radius of 500 μm is of the order of 2 MPa.

The results indicate that untreated silk films can be imprinted over a wide process window of contact stresses, from less than 2 MPa to a maximum of 100 MPa, at room temperature. It is quite possible that the film may be imprintable at contact stresses below 2 MPa, as small variations in the film properties or other inaccuracies in the computation could significantly alter this small number. Indeed, we have reported the ability to nanoimprint similar silk films at a pressure of 0.35 MPa (50 psi) at 80–100 °C in times of the order of 5 s [10, 11]. The stresses computed here are approximate, as they rely on an elastic/plastic quasistatic material model that does not include viscoelastic properties of the silk or vibration and wave motion that may occur during impact.

Conclusions

Rapid nano impact printing has been demonstrated, characterized, and modeled for the imprinting of 2 μm diameter, 100–200 nm wide rings into untreated silk thin films. The impact itself occurs in less than 1 ms, and the entire impact printing operation can be accomplished within 100 ms. It is the rapid nature of the printing process that is most unique. By confining the pattern transfer to the impact event, nanoscale patterns can be transferred more rapidly than by micromolding or traditional nanoimprinting.

The details of the impact event are important for determining the local contact stresses which drive the pattern transfer process. These local stresses will depend on the geometry of the imprinter and the material properties of the film. This could be cause for concern, since it might be difficult to control the stresses during the impact. However, in this work we have shown that for silk biopolymer thin films, the process window is wide, extending from below 2–100 MPa. This suggests that pattern transfer during the impact can be robust. Small area, repeatable pattern transfer into silk has been demonstrated as an example of this, and has been shown to be relatively insensitive to temperature.

In addition to the impact printing process, the demonstration of the ability to nano impact print into silk biopolymer thin films is important. The unique mechanical, chemical, optical, and biocompatible properties of silk make it an attractive material, particularly for biomedical and biophotonic devices. Nano impact printing may prove to be a useful tool for the manufacturing of silk devices, particularly in manufacturing environments that require high throughput or flexible local patterning.

Additional work is needed to characterize the ability of nano impact printing to operate over large areas. In this work, a hemispherical indenter was used in order to allow the investigation of a range of contact stresses during a single experiment. However, now that the optimal contact stress process window is known, an impact printer can be designed to operate exclusively in this window, and to produce larger areas of pattern transfer during a single impact. It will be important to characterize and analyze the uniformity and repeatability of the process. In addition, more work should be done on the microscale heat generation and conduction during the impact event. Better knowledge of any local heating that may occur is needed, coupled to evaluation of any effects local heating could have on the properties of the biopolymer film or any dopants.

References

[1] Altman G H, Diaz F, Jakuba C, Calabro T, Horan R L, Chen J, Lu H, Richmond J and Kaplan D L 2003 Silk-based biomaterials *Biomaterials* **24** 401–16
[2] Omenetto F G and Kaplan D L 2008 A new route for silk *Nature Photonics* **2** 641–3
[3] Arai T, Freddi G, Innocenti R and Tsukada M 2004 Biodegradation of *Bombyx mori* silk fibroin fibers and films *J. Appl. Polym. Sci.* **91** 2383–90
[4] Kim U J, Park J, Kim H J, Wada M and Kaplan D L 2005 Three-dimensional aqueous-derived biomaterial scaffolds from silk fibroin *Biomaterials* **26** 2775–85
[5] Lawrence B D, Omenetto F, Chui K and Kaplan D L 2008 Processing methods to control silk fibroin film biomaterial features *J. Mater. Sci.* **43** 6967–85
[6] Demura M and Asakura T 1989 Immobilization of glucose oxidase with *Bombyx mori* silk fibroin by only stretching treatment and its application to glucose sensor *Biotechnol. Bioeng.* **33** 598–603
[7] Lawrence B D, Cronin-Golomb M, Georgakoudi I, Kaplan D L and Omenetto F G 2008 Bioactive silk protein biomaterial systems for optical devices *Biomacromolecules* **9** 1214–20
[8] Lu S, Wang X, Lu Q, Hu X, Uppal N, Omenetto F G and Kaplan D L 2009 Stabilization of enzymes in silk films *Biomacromolecules* **10** 217–26
[9] Perry H, Gopinath A, Kaplan D L, Negro L D and Omenetto F G 2008 Nano-and micropatterning of optically transparent, mechanically robust, biocompatible silk fibroin films *Adv. Mater.* **20** 3070–2
[10] Amsden J J, Domachuk P, Gopinath A, White R D, Negro L D, Kaplan D L and Omenetto F G 2010 Rapid nanoimprinting of silk fibroin films for biophotonic applications *Adv. Mater.* **22** 1746–9
[11] Mondia J P, Amsden J J, Lin D, Negro L D, Kaplan D L and Omenetto F G 2010 Rapid nanoimprinting of doped silk films for enhanced fluorescent emission *Adv. Mater.* **22** 4596–9
[12] Chou S Y, Krauss P R and Renstrom P J 1995 Imprint of sub 25 nm vias and trenches in polymers *Appl. Phys. Lett.* **67** 3114
[13] Chou S Y, Krauss P R and Renstrom P J 1996 Imprint lithography with 25-nanometer resolution *Science* **272** 85
[14] Chou S Y, Krauss P R, Zhang W, Guo L and Zhuang L 1997 Sub-10 nm imprint lithography and applications *J. Vac. Sci. Technol.* B **15** 2897–904
[15] Park I, Cheng J, Pisano A P, Lee E S and Jeong J H 2007 Low temperature, low pressure nanoimprinting of chitosan as a biomaterial for bionanotechnology applications *Appl. Phys. Lett.* **90** 093902
[16] Jin H, Park J, Karageorgiou V, Kim U, Valluzzi R, Cebe P and Kaplan D L 2005 Water-stable silk films with reduced beta-sheet content *Adv. Funct. Mater.* **15** 1241
[17] Budynas R G 1999 *Advanced Strength and Applied Stress Analysis* (New York: McGraw-Hill)
[18] Hertz H 1881 Über die Berührung fester elastischer Körper *J. Reine Angew. Math.* **92** 156–71

[19] Jackson R L and Green I 2005 A finite element study of elasto-plastic hemispherical contact against a rigid flat *Trans. ASME, J. Tribol.* **127** 343–54

[20] Laconte J, Flandre D and Raskin J P 2006 *Micromachined Thin-Film Sensors for SOI-CMOS Co-Integration* (The Netherlands: Springer)

[21] Marshall J C, Herman D L, Vernier P T, DeVoe D L and Gaitan M 2007 Young's modulus measurements in standard IC CMOS processes using MEMS test structures *IEEE Electron Device Lett.* **28** 960–3

[22] Cease H, Derwent P F, Diehl H T, Fast J and Finley D 2006 Measurement of mechanical properties of three epoxy adhesives at cryogenic temperatures for CCD construction *Fermi National Accelerator Laboratory*

[23] Pérez-Rigueiro J, Viney C, Llorca J and Elices M 2000 Mechanical properties of silkworm silk in liquid media *Polymer* **41** 8433–9

[24] Jiang C, Wang X, Gunawidjaja R, Lin Y H, Gupta M K, Kaplan D L, Naik R R and Tsukruk V V 2007 Mechanical properties of robust ultrathin silk fibroin films *Adv. Funct. Mater.* **17** 2229

[25] Noishiki Y, Nishiyama Y, Wada M, Kuga S and Magoshi J 2002 Mechanical properties of silk fibroin-microcrystalline cellulose composite films *J. Appl. Polym. Sci.* **86** 3425–9

[26] Tsuboi Y, Goto M and Itaya A 2001 Pulsed laser deposition of silk protein: effect of photosensitized-ablation on the secondary structure in thin deposited films *J. Appl. Phys.* **89** 7917